IEEE Robotics and Automation Letters (RA-L) paper, presented at ICRA 2026, Vienna, Austria. Cite as RA-L paper.

Orthogonal Pulse-Width-Modulation for Combined Electromagnetic Actuation and Localization

Denis von Arx, *Graduate Student Member, IEEE*, Bradley J. Nelson, *Fellow, IEEE*, and Quentin Boehler, *Senior Member, IEEE*

***Abstract*—Electromagnetic Navigation Systems can be used to remotely guide medical devices such as magnetic catheters or guidewires, holding potential in a variety of minimally invasive surgical applications. This paper introduces a method to simultaneously actuate and localize a tethered magnetic device with embedded sensor pickup coils using a single system. Six-degree-of-freedom localization is achieved by driving the electromagnets of the Electromagnetic Navigation System with mutually orthogonal pulse-width-modulated voltages of different frequencies. The method is demonstrated using a human-scale system composed of three electromagnets to actuate and localize a magnetic catheter prototype with pickup coils embedded at its tip. In this case, the pose is estimated at a rate of 77 Hz, with a typical mean accuracy below 2 mm in position and 2° in orientation.**

***Index Terms*—Localization, Surgical Robotics: Steerable Catheters/Needles, Remote Magnetic Navigation, Electromagnetic Tracking**

I. Introduction

ELECTROMAGNETIC navigation systems (eMNS) have gathered widespread interest from researchers in recent years due to their ability to control magnetic catheters and guidewires, enabling increased automation and dexterity in a variety of minimally invasive procedures [1]. These systems are composed of current-controlled electromagnets that generate magnetic fields to apply forces and torques remotely on a device containing magnetic materials [2].

Accurate and real-time feedback on the pose of the magnetic device navigated within the human body is crucial, and combined actuation and six-degree-of-freedom (DoF) localization using magnetic fields have received significant research attention. Existing methods for simultaneous magnetic actuation and localization rely on a combination of embedded sensors such as multiple Hall effect sensors [3] or on their combination with inertial measurement units [4]–[8] to estimate the pose of the device based on static or dynamic magnetic fields produced by moving permanent magnets or electromagnetic coils. The usage of multiple sensors puts limitations on the miniaturization of such approaches, which may be necessary for integration into medical tools such as catheters or guidewires. Localization can also be achieved using external sensor arrays [9] to sense the field of the actuated magnet, but the range of such methods is limited by the size of the magnet under actuation.

Previous work on localizing a single three-axis Hall effect sensor in tethered devices at rates of up to 10 Hz has been reported in [10], [11]. In [10], authors report localization errors of $5.65\,\mathrm{mm}$ in position in 2D space, and relied on additional geometrical information about the vasculature. In [11], small oscillating fields for localization are superimposed onto quasi-static actuation fields, leading to errors of $1\,\mathrm{mm}$ and $2°$.

Generating AC fields of sufficient signal-to-noise ratio (SNR) for such a Hall-effect-based localization requires that a significant amount of reactive power be transmitted to the electromagnets. This problem is worsened by the fact that the Hall sensor range must be chosen high enough to avoid saturation, thus reducing SNR for higher magnitude actuation fields. In [11], this issue was mitigated by using comparatively small electromagnets and low oscillation frequencies, which limits the magnitude and range of the field and can lead to vibrations of the permanent magnets subjected to the magnetic fields.

In addition to Hall effect-based localization, electromagnetic tracking (EMT) based on inductive pickup coils is commonly used for tracking medical devices in the absence of line-of-sight [12], [13]. EMT consists of localizing sensor pickup coils embedded in the device by emitting AC fields in space and measuring the pose-dependent voltages induced in the coils. Since pickup coils react to the time derivative of the field, they cannot be saturated by the actuation fields, and they can work with very small field magnitudes. This leads to higher SNR and lower reactive power requirements in combined actuation and localization applications compared to methods using Hall effect sensors.

The field generated by an eMNS naturally includes high frequency components, referred to as *magnetic ripple fields*, which originate from the pulse-width-modulation (PWM) employed in the power electronic converters that drive the currents of the electromagnets. The method we introduce in this work leverages this property to estimate the pose of a tethered magnetic device. This is achieved by measuring the ripple fields using pickup coils attached to a permanent magnet at the distal tip of the device. Each of the electromagnets is driven with synchronous PWM of different frequencies that share a common period to ensure a periodic ripple field throughout space. Our method allows us to both actuate and localize the tip of the device, combining the advantages of electromagnetic actuation and EMT in a single system.

Electromagnets employed in an eMNS are usually larger than

Manuscript received January 9, 2025; Revised March 27, 2025; Accepted May 2, 2025.

This paper was recommended for publication by Editor Pietro Valdastri upon evaluation of the Associate Editor and Reviewers' comments.

This work was supported by he Swiss National Science Foundation through grant number 200020_212885, and the ITC-InnoHK grant 16312.

The authors are with the Multi-Scale Robotics Lab, ETH Zurich, Switzerland; {dvarx,bnelson,qboehler}@ethz.ch

Digital Object Identifier (DOI): see top of this page.

IEEE Robotics and Automation Letters (RA-L) paper, presented at ICRA 2026, Vienna, Austria. Cite as RA-L paper.

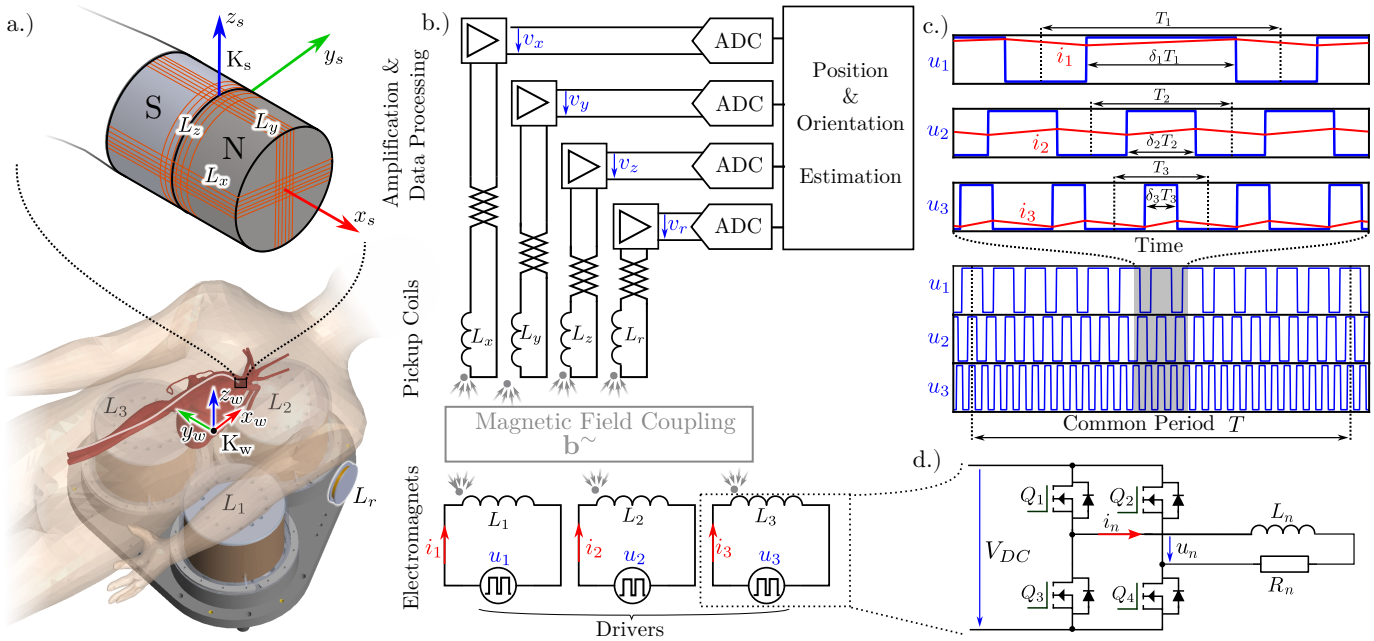

Fig. 1: Overview of the method for combined electromagnetic actuation and localization. a.) Magnetic catheter actuated by an electromagnetic navigation system composed of three electromagnets (L_1 to L_3). The sensor composed of three pickup coils (L_x, L_y and L_z) is attached to the magnetic tip, and a reference pickup coil L_r is attached to the system. b.) Magnetic coupling between PWM driven electromagnets and pickup coils. c.) Voltage waveforms of the orthogonal PWM scheme d.) H-bridge circuit used to the drive electromagnets and generate the PWM waveforms.

the field emitters used in commercial EMT systems and are driven with higher power. This results in magnetic ripple fields that are large enough such that the method can achieve acceptable SNR with less sensitive inductive sensors that do not feature a soft magnetic core which is commonly used to increase pickup coil sensitivity [14]. Instead, the pickup coils can be directly attached to the permanent magnet to be actuated which allows for space saving integration into a magnetically actuated, tethered device. Compared to previously reported methods [10], [11], this approach does require neither additional geometrical information nor the transfer of significant reactive power.

The experimental validation of the method is performed on a human-scale, three-electromagnet eMNS with three-axis pickup coils (Fig. 1a). Realistic actuation and localization tasks are demonstrated by embedding the pickup coils at the tip of a magnetic catheter to navigate both in free space, and in a phantom of the human vasculature.

II. Method

A. Electromagnetic Navigation

We consider an eMNS comprising M electromagnets L_m with $m \in \{1, \dots, M\}$, which at any position $\mathbf{p} \in \mathbb{R}^3$ generate an actuation field $\mathbf{b}^a(\mathbf{p}) \in \mathbb{R}^3$ to induce a torque and force on a permanent magnet attached to the tip of a flexible tool such as a catheter as shown in Fig. 1a.

Assuming a linear relationship between each electromagnet's current i_m and the generated field [2], the currents to achieve a desired actuation field at $\mathbf{p}$ are computed as

$$\mathbf{i} = \mathbf{A}^{\dagger}(\mathbf{p})\mathbf{b}^a(\mathbf{p}) \tag{1}$$

where $\mathbf{A}^{\dagger}$ is the Moore-Penrose pseudoinverse of a position-dependent actuation matrix $\mathbf{A}(\mathbf{p}) \in \mathbb{R}^{3\times M}$, and $\mathbf{i}$ is a current vector so that $\mathbf{i} = \begin{bmatrix} i_1 & \cdots & i_M \end{bmatrix}^T$. In this paper, we consider an eMNS composed of $M = 3$ electromagnets (see Fig. 1a), but the the method we introduce in the following is valid for an arbitrary number of electromagnets $M \geq 3$.

B. Orthogonal Pulse Width Modulation

Each current i_m is generated by a driver which applies a pulse-width modulated (PWM) voltage u_m to the electromagnet L_m as shown in Fig. 1b-d. The output voltages are generated by switching the power electronic switches in an H-bridge circuit (see Fig. 1d). The localization method relies on the fact that a different PWM frequency is used for each driver of the system. The PWM frequencies are chosen such that the PWM signals share a common period T defined as the least common multiple of (T_1, T_2, T_3) where T_m is the period of the PWM signal driving L_m (see Fig. 1c). It is further assumed that none of the PWM frequencies is a multiple of another. This modulation scheme is referred to as *orthogonal PWM* since all of the harmonics of the PWM signals are mutually orthogonal functions on the time interval $[0, T]$. This property is used here to separate small field ripples caused by the PWM in the frequency domain (see Section II-C), and it forms the basis of the proposed localization method. The output voltage u_m of a driver consists of the sum of a DC component $u_m^-(\delta_m)$, and an AC component $u_m^{\sim}(\delta_m)$:

$$u_m^-(\delta_m) = V_{DC}[1 - 2\delta_m] \tag{2a}$$

$$u_m^{\sim}(\delta_m) = \frac{4V_{DC}}{\pi} \sum_{n=1}^{\infty} \frac{\sin(n\pi\delta_m)}{n} \cos(n\omega_m t) \tag{2b}$$

IEEE Robotics and Automation Letters (RA-L) paper, presented at ICRA 2026, Vienna, Austria. Cite as RA-L paper.

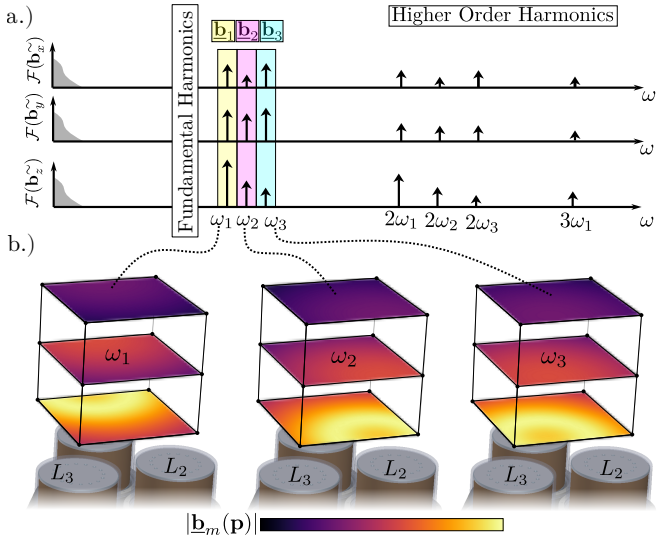

Fig. 2: Magnetic ripple field for an electromagnetic navigation system composed of three electromagnets. a.) Spectra of the magnetic ripple field components $\{\mathbf{b}_x^{\sim}, \mathbf{b}_y^{\sim}, \mathbf{b}_z^{\sim}\}$ b.) Magnitudes of the fundamental components of the magnetic ripple field $\mathbf{b}^{\sim}$ throughout the workspace.

where V_{DC} is the DC link voltage connected to the drivers (see Fig. 1d), $\omega_m = 2\pi/T_m$ are the PWM frequencies, and $\delta_m \in (0, 1)$ are the duty cycles of the PWM waveforms. The duty cycles δ_m determine the mean voltages applied to the electromagnets (Eq. (2a)) which are used to control the slowly varying actuation currents i_m. According to Eq. (2b), changing these mean voltages also changes the AC parts of the voltages that generate the fields used for localization as discussed in the next section. To compensate for this effect, measurements from a reference sensor L_r in the vicinity of the eMNS are used (see Fig. 1a). In the cases $\delta_m \in \{0, 1\}$, no AC voltage components are generated, and it is therefore assumed that the outputs of the H-bridge legs are pulled neither permanently high or low.

C. Magnetic Ripple Field

The AC components $u_m^{\sim}$ of the PWM voltages result in corresponding current ripples (see Fig. 1c), and therefore in a magnetic ripple field throughout the workspace of the eMNS. The magnetic ripple field at position $\mathbf{p}$ and time t is expressed as

$$\mathbf{b}^{\sim}(\mathbf{p}, t) = \sum_{m=1}^{M} \sum_{n=1}^{\infty} \mathrm{Re}\{\underline{\mathbf{b}}_{m,n}(\mathbf{p}) e^{jn\omega_m t}\} \tag{3}$$

and it consists of harmonics at the frequencies $n\omega_m$. The quantity $\underline{\mathbf{b}}_{m,n}(\mathbf{p}) \in \mathbb{C}^3$ is a vector of phasors referred to as the *field harmonic* at frequency $n\omega_m$. A typical spectrum of the ripple field at an arbitrary position in the workspace of the three-electromagnet eMNS is shown in Fig. 2a.

The localization method relies on measuring the fundamental field harmonics $\underline{\mathbf{b}}_m(\mathbf{p}) = \underline{\mathbf{b}}_{m,1}(\mathbf{p})$ using a sensor composed of three orthogonal pickup coils $\{L_x, L_y, L_z\}$ attached to the permanent magnet under actuation as shown in Fig. 1a. Only the fundamental frequencies are used since they form the largest components of the ripple field according to Eq. (2b), and thus provide the highest SNR. The intensity of the field harmonics at the fundamental frequencies $\{\omega_1, \omega_2, \omega_3\}$ throughout the workspace of the three-electromagnet eMNS considered in this work is shown in Fig. 2b. These fundamental field harmonics are unique to any pose in space, and the localization of the sensors therefore consists in solving an optimization problem comparing the measurements at the pose to be determined, to calibration data acquired at known poses.

D. Pickup Coils Measurement

The field harmonics induce voltages in the pickup coils which are amplified resulting in the voltages $\{v_x, v_y, v_z\}$ as shown in Fig. 1b. The sensor is assumed to be a linear and time invariant (LTI) system, so that the voltages in the pickup coils are related to the fundamental field harmonics according to:

$$\underline{\mathbf{v}}_m = \mathbf{S}(\omega_m)\, {}^{\mathrm{K_s}}\underline{\mathbf{b}}_m \tag{4}$$

where $\underline{\mathbf{v}}_m = [\underline{v}_{x,m}, \underline{v}_{y,m}, \underline{v}_{z,m}]^T \in \mathbb{C}^3$ are vectors containing the phasors of the ω_m-components of the pickup coil voltage, ${}^{\mathrm{K_s}}\underline{\mathbf{b}}_m$ are the fundamental field harmonics expressed in the coordinate system $\mathrm{K_s}$ attached to the sensor (see Fig. 1a), and $\mathbf{S}(\omega_m) \in \mathbb{C}^{3\times3}$ is referred to as a *sensitivity matrix* whose value is nominally given by

$$\mathbf{S}(\omega_m) = j\omega_m G(\omega_m) \mathrm{diag}(N_x A_x, N_y A_y, N_z A_z) \tag{5}$$

with $G(\omega_m)$ the amplifier gain and N_x, A_x etc. the turn numbers and areas of the pickup coils. Due to imperfections in the manufacturing of the pickup coils, $\mathbf{S}(\omega_m)$ typically has to be determined empirically. An experimental method on how to do so using a Helmholtz coil is described in Section III-B. The ripple field in the workspace changes over time due to changing actuation fields or fluctuating DC link voltage according to Eq. (2b). To model this influence, we assume an LTI system with inputs being the voltages $u_m^{\sim}$, and outputs being the sensor voltage $\{v_x, v_y, v_z\}$. Under this assumption, measuring the field harmonics $\underline{\mathbf{b}}_m(\mathbf{p}, t_0)$ at a time t_0 allows to predict these fundamental field harmonics at any other time t_1 as

$$\underline{\mathbf{b}}_m(\mathbf{p}, t_1) = \underline{\mathbf{b}}_m(\mathbf{p}, t_0) \cdot \frac{\underline{v}_{r,m}(t_1)}{\underline{v}_{r,m}(t_0)} \tag{6}$$

where $\underline{v}_{r,m}(t)$ is the phasor of the ω_m-component of the reference pickup coil (L_r in Fig. 1a) voltage estimated at time t. L_r is placed outside the eMNS workspace but close enough such that its SNR does not significantly degrade the field prediction in (6).

E. Pose Estimation

The pose of the sensor is estimated following the steps outlined in Fig. 3. They consist of estimating the fundamental field harmonics at the sensor location, and comparing these measurements to previously obtained maps of these harmonics generated by the eMNS across space.

1) Field Phasor Estimation: Given Eq. (4), the fundamental field harmonics at the pose of the sensor are first estimated from the pickup coil voltages. The voltages $\{v_x, v_y, v_z\}$ are sampled at a rate f_s and buffered in vectors $\{\mathbf{v}_x, \mathbf{v}_y, \mathbf{v}_z\} \in \mathbb{R}^{N_s}$ that each hold N_s samples. From these buffers, the voltage

IEEE Robotics and Automation Letters (RA-L) paper, presented at ICRA 2026, Vienna, Austria. Cite as RA-L paper.

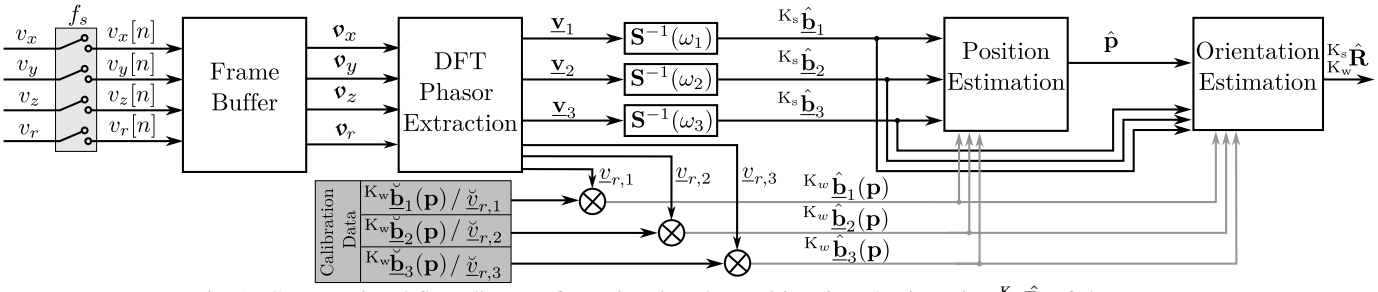

Fig. 3: Computational flow diagram for estimating the position $\hat{\mathbf{p}}$ and orientation ${}^{\mathrm{K_s}}_{\mathrm{K_w}}\hat{\mathbf{R}}$ of the sensor.

phasor vectors are estimated using a discrete Fourier transform (DFT):

$$\underline{\mathbf{v}}_m = \frac{1}{N_s}\begin{bmatrix}\mathrm{DFT}(\boldsymbol{v}_x)[k_m]\\ \mathrm{DFT}(\boldsymbol{v}_y)[k_m]\\ \mathrm{DFT}(\boldsymbol{v}_z)[k_m]\end{bmatrix} \tag{7}$$

where $k_m = \frac{\omega_m N_s}{2\pi f_s}$ are the discrete frequencies corresponding to ω_m. An estimate ${}^{\mathrm{K_s}}\hat{\underline{\mathbf{b}}}_m$ for the fundamental field harmonics in $\mathrm{K_s}$ is then computed by multiplying the voltage phasors $\underline{\mathbf{v}}_m$ by the inverse sensitivity matrices $\mathbf{S}^{-1}(\omega_m)$ according to Eq. (4).

2) Magnetic Ripple Fields Calibration: The fundamental field harmonics $\underline{\mathbf{b}}_m(\mathbf{p})$ are sampled throughout the workspace at each point of a calibration grid. During calibration, the coordinate system $\mathrm{K_s}$ is aligned with $\mathrm{K_w}$, a "world" coordinate system attached to the eMNS (see Fig. 1a), and zero actuation fields are applied for this calibration measurement (i.e. $\delta_m = 0.5$). The fields can then be interpolated from this data at any position $\mathbf{p}$ to estimate calibration fieldmaps ${}^{\mathrm{K_w}}\breve{\underline{\mathbf{b}}}_m(\mathbf{p})$ describing the fields throughout the entire workspace of the eMNS. These fieldmaps are given in $\mathrm{K_w}$ and stored as calibration data. The reference sensor voltage phasors $\breve{\underline{v}}_{r,m}$ at the fundamental frequencies are stored as well during the calibration procedure.

3) Fieldmap Estimation: The fundamental fields harmonics at any position $\mathbf{p}$ are estimated from the calibration fieldmaps by multiplication with the correction factors derived from the reference sensor phasors (see Eq. (6)):

$${}^{\mathrm{K_w}}\hat{\underline{\mathbf{b}}}_m(\mathbf{p}) = {}^{\mathrm{K_w}}\breve{\underline{\mathbf{b}}}_m(\mathbf{p}) \cdot \frac{\underline{v}_{r,m}}{\breve{\underline{v}}_{r,m}} \tag{8}$$

4) Position Estimation: To estimate the position $\hat{\mathbf{p}}$ of the sensor, the magnitudes of the fields ${}^{\mathrm{K_s}}\hat{\underline{\mathbf{b}}}_m$ measured by the sensor are compared to the fieldmaps by solving the following optimization problem:

$$\hat{\mathbf{p}} = \underset{\mathbf{p}}{\operatorname{argmin}} \sum_{m=1}^{M} \left(|{}^{\mathrm{K_s}}\hat{\underline{\mathbf{b}}}_m| - |{}^{\mathrm{K_w}}\hat{\underline{\mathbf{b}}}_m(\mathbf{p})| \right)^2 \tag{9}$$

5) Orientation Estimation: The fundamental field harmonics expressed in $\mathrm{K_w}$ are then estimated at $\hat{\mathbf{p}}$ from the fieldmaps (see Eq. 8), and the orientation of $\mathrm{K_s}$ in coordinates of $\mathrm{K_w}$ is then estimated as the rotation matrix

$${}^{\mathrm{K_s}}_{\mathrm{K_w}}\hat{\mathbf{R}} = \underset{\mathbf{R}\in SO(3)}{\operatorname{argmin}} \left\| \mathbf{R}\left[{}^{\mathrm{K_w}}\hat{\underline{\mathbf{b}}}_1(\hat{\mathbf{p}}), \cdots, {}^{\mathrm{K_w}}\hat{\underline{\mathbf{b}}}_M(\hat{\mathbf{p}}) \right] - \left[{}^{\mathrm{K_s}}\hat{\underline{\mathbf{b}}}_1, \cdots, {}^{\mathrm{K_s}}\hat{\underline{\mathbf{b}}}_M \right] \right\|_F \tag{10}$$

which is computed as the solution of a Procrustes problem introduced in Appendix B in [11].

III. Experimental Results

A. Experimental Setup

The method was evaluated using the setup depicted in Fig. 4a. The eMNS consists of three electromagnets driven by H-bridge circuits controlled by a TMDSCNCD28388D control card from Texas Instruments. The drivers are fed by a 120 V supply with a maximum power of 2.4 kW. The PWM modules of the microcontroller were configured to implement orthogonal PWM of frequencies $\{9.7, 8.1, 7.0\}$ kHz with a common period $T \approx 4.3$ ms. These frequencies are in range of reported EMT systems such as [13]. The sensor voltages were measured during an acquisition time interval of $T_{acq} = 10$ ms as shown in Fig. 4b. This allowed for computing a new pose estimate every $3T \approx 12.9$ ms resulting in an effective localization rate of 77 Hz.

A three-axis gantry stage driven by stepper motors was used to cover a cubic volume $\mathcal{V}$ of sidelength 30 cm located 7 cm from the electromagnets (see Fig. 2b). To acquire the calibration fieldmaps described in Section II-E2, the pickup coils were rigidly mounted at the end effector of the stage. The workspace volume was sampled using a regular 16×16×16 grid with unit cell length 2 cm. The interpolation of the fields was done using tricubic interpolation from the `scipy.interpolate` package. The localization problem (9) was solved using `least_squares` from `scipy.optimize`. Computation time for the position estimation was 8.5 ms.

The signals from the pickup coils were amplified using the circuit depicted in Fig. 4c. It consists of four identical channels consisting of a low noise instrumentation amplifier (AD8429) followed by a variable gain stage (AD8033) and a differential ADC driver (THP210). An USB 1808-GX DAQ device (Measurement Computing) was used to sample the output signals at $f_s = 200$ kHz. Each dataframe of 10 ms therefore contained $4 \times N_s$ samples, with $N_s = 2000$.

The pickup coils were wrapped around a NdFeB permanent magnet with a diameter and height of 4 mm (see Fig. 4d).

IEEE Robotics and Automation Letters (RA-L) paper, presented at ICRA 2026, Vienna, Austria. Cite as RA-L paper.

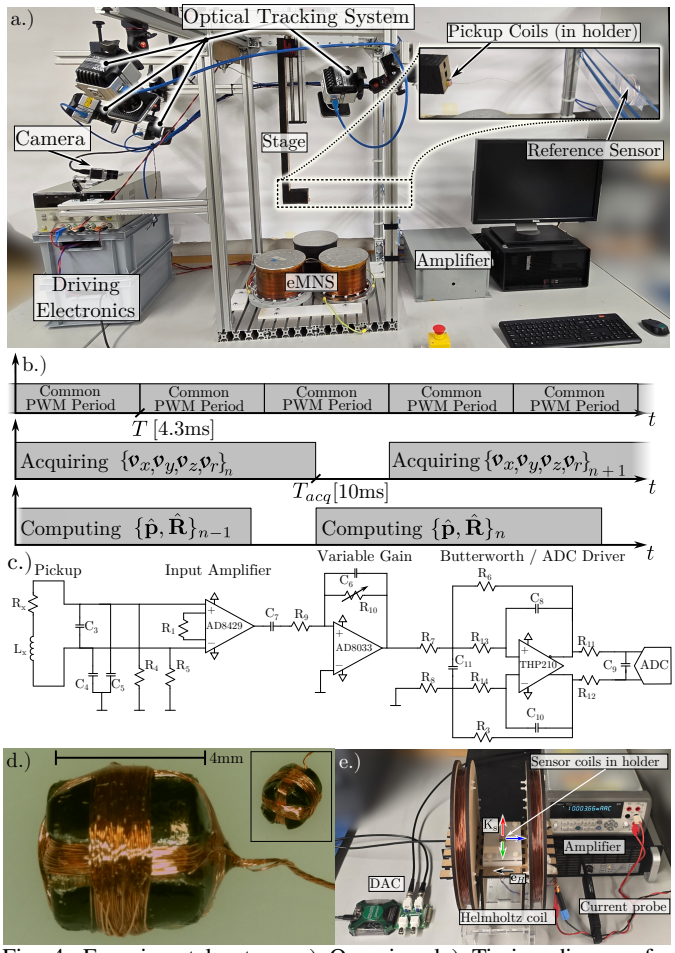

Fig. 4: Experimental setup. a.) Overview b.) Timing diagram for frame acquisition and pose estimation c.) Amplifier circuit schematic for each of the pickup coils d.) Pickup coils embedded on a permanent magnet e.) Sensor calibration setup.

Small grooves were cut into the sides of the magnet using an engraving pen to accommodate the L_x and L_y pickup coils. Approximately 100 turns of $50\,\mu\text{m}$ enameled wire could be fit in this available space. The L_z pickup coil was wound along the diameter with a similar number of turns. The six wire leads were twisted to minimize spurious induction as described in [15]. The sensors sensitivity matrix was calibrated using the setup depicted in Fig. 4e as described in Section III-B.

An optical tracking system (OTS, Vicon Motion Systems Ltd) was attached to the setup to measure the ground truth poses of the pickup coils when required by the experiment (see Sections III-C3 and III-D1). The reported accuracy of the OTS is $0.35\,\text{mm} \pm 0.24\,\text{mm}$ for the velocities used in the experiments [16]. An additional camera registered to the OTS was used to visualize the motion of the sensor with an overlay of the pose estimates in these cases.

B. Sensor Calibration

The sensor calibration consists of determining the sensitivity matrix $\mathbf{S}(\omega_m)$ at the fundamental frequencies ω_m (see Section II-D). The sensor was placed in a Helmholtz coil (see Fig. 4e) and exposed to a field that was generated by

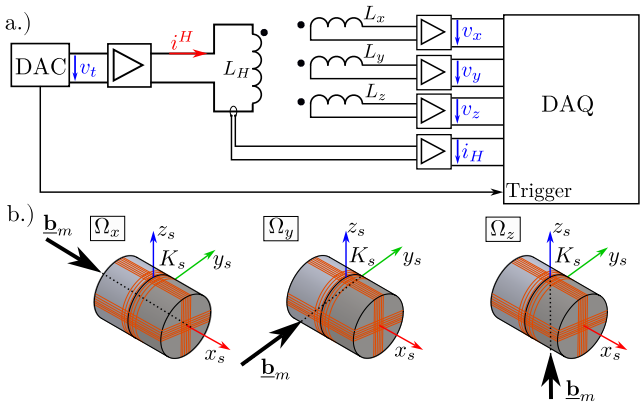

Fig. 5: Sensor calibration. a.) Circuit of the calibration setup using a Helmholtz coil L_H. b.) Orientations during the calibration measurements $\{\Omega_x, \Omega_y, \Omega_z\}$.

amplifying a test voltage (see Fig. 5a)

$$v_t = \sum_m \text{Re}\{\underline{v}_{t,m} e^{j\omega_m t}\} \tag{11}$$

which contains the components $\underline{v}_{t,m}$ at the PWM fundamental frequencies ω_m. This exposed the sensor to a field

$$\mathbf{b}(t) = \beta \mathbf{e}_H \sum_m \text{Re}\{\underline{i}_m^H e^{j\omega_m t}\} \tag{12}$$

where $\underline{i}_m^H$ are the current components of frequencies ω_m flowing in the Helmholtz coil, β is the gain of the Helmholtz coil in units of [T/A], and $\mathbf{e}_H$ is a unit vector along the Helmholtz coil axis. Three experiments $\{\Omega_x, \Omega_y, \Omega_z\}$ were conducted by placing the sensor such that a different sensor axis faced the field each time (see Fig. 5b). This resulted in the measured voltages vectors $\{\underline{\mathbf{v}}_m^{\Omega_x}, \underline{\mathbf{v}}_m^{\Omega_y}, \underline{\mathbf{v}}_m^{\Omega_z}\} \in \mathbb{C}^3$. The current components $\underline{i}_m^H$ were measured as well and were kept constant through the experiments. Applying Eq. (4) to the three measured voltage vectors yields the following relationship:

$$[\underline{\mathbf{v}}_m^{\Omega_x}, \underline{\mathbf{v}}_m^{\Omega_y}, \underline{\mathbf{v}}_m^{\Omega_z}] = \mathbf{S}(\omega_m)\beta \underline{i}_m^H \tag{13}$$

The above equation allows to directly calculate the sensitivity matrix at the fundamental frequencies from the measured voltage phasor vectors and the measured current phasors.

C. Localization Performance

1) Evaluation Metrics: The error $e_\mathbf{p}$ on the position estimate is defined as the Euclidean distance between the ground truth position and its estimate $\hat{\mathbf{p}}$. The error $e_\mathbf{R}$ on the rotation matrix estimating the orientation is defined as the geodesic error [17]:

$$e_\mathbf{R} = \left\| \log\left({}^{\text{K}_\text{s}}_{\text{K}_\text{w}}\hat{\mathbf{R}}^T \mathbf{R} \right) \right\|_2 \tag{14}$$

with $\mathbf{R}$ the ground truth rotation matrix. To calculate the position accuracy $\mu_\mathbf{p}$ and orientation accuracy $\mu_\mathbf{R}$, 128 estimates of $\hat{\mathbf{p}}$ and ${}^{\text{K}_\text{s}}_{\text{K}_\text{w}}\hat{\mathbf{R}}$ were averaged for each test position to reduce the influence of measurement noise. To compute the position precision $\sigma_\mathbf{p}$ and orientation precision $\sigma_\mathbf{R}$, deviations from the mean estimates were computed and the RMS value of these deviations was calculated.

IEEE Robotics and Automation Letters (RA-L) paper, presented at ICRA 2026, Vienna, Austria. Cite as RA-L paper.

2) 3-DoF Motion on Test Grid: Localization accuracy and precision are first evaluated without actuation ($\delta_m = 0.5$). The sensor was attached in a fixed orientation to the gantry stage used to acquire the calibration data, and test points on a $15\times15\times15$ regular grid with sidelength $2\,\mathrm{cm}$ were localized resulting in 3375 test points located in between calibration grid points. The resulting accuracy and precision distributions are plotted in Fig. 6. The mean position estimate accuracy and precision in $\mathcal{V}$ were $0.49\,\mathrm{mm}$ and $0.42\,\mathrm{mm}$ respectively. The accuracy distribution showed an offset of $0.4\,\mathrm{mm}$ which was attributed to experimental limitations related to the gantry stage setup. The mean accuracy and precision of the orientation estimate were respectively evaluated as $0.28°$ and $0.12°$.

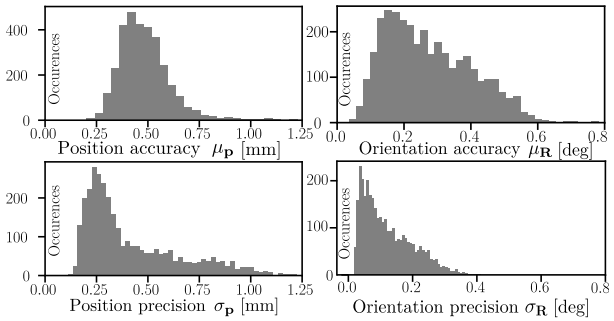

Fig. 6: Localization performance on a test grid without actuation field. a.) Position estimate accuracy $\mu_\mathbf{p}$ and precision $\sigma_\mathbf{p}$ throughout the workspace b.) Orientation accuracy $\mu_\mathbf{R}$ and precision $\sigma_\mathbf{R}$ throughout the workspace.

3) 6-DoF Motion in Free Space: To evaluate the accuracy for different orientations, the sensor was attached to a structure embedding optical fiducials that allowed for tracking the pose of the structure using the OTS. The structure was then manually moved in the workspace to sample different orientations and positions. Five experiments were conducted to determine values for the position and orientation accuracy. Figure 7a shows a typical trajectory of the sensor in the workspace. In this experiment, the orientation of the sensor is described using the Euler angles (α, β, γ) as defined in Fig. 7b. The mean position and orientation estimate accuracies for the experiments were determined as $1.2\,\mathrm{mm}$ and $1.1°$ respectively. Figure 7c shows the coordinate trajectories for one experiment. It shows an $e_\mathbf{p}$ with a mean of $1.02\,\mathrm{mm}$ and a maximum of $4.33\,\mathrm{mm}$ with an IQR of $0.62\,\mathrm{mm}$. $e_\mathbf{R}$ shows a mean of $1.72°$ and a maximum of $4.51°$ with an IQR of $1.34°$. A Procrustes analysis without scaling was performed on the position estimates of the eMNS and OTS to compute the positional error. The orientation error was calculated using the orientation relative to the initial orientation at the beginning of the experiment and Eq. (14).

4) Precision and Scaling Considerations: Figure 8 shows the measured signal spectra at the center of $\mathcal{V}$. For the given sensor, the input noise floor is mainly made up of the input amplifier noise and the thermal resistor noise from the pickup coils. Both contributed approximately $0.9\,\mathrm{nV}/\sqrt{\mathrm{Hz}}$. For smaller sensors than the ones used in this work, the thermal contribution to the sensor noise $\nu_{rms}^{th} \sim \sqrt{R}$, with R the resistance of the pickup coils, would dominate due to

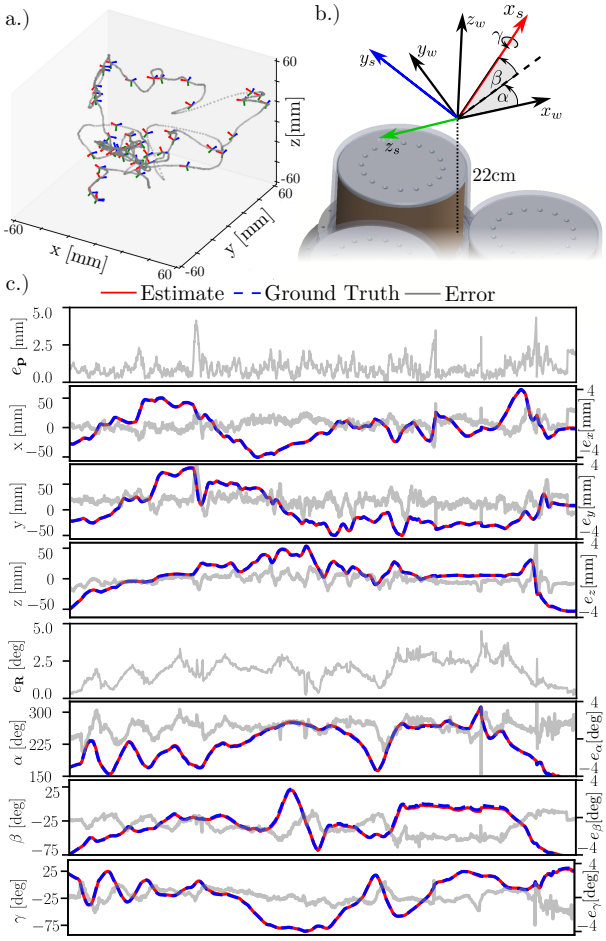

Fig. 7: Pose estimation when manually moving the sensor in the workspace with 6 DoF, with relative errors on each DoF. a.) Trajectory of sensor in workspace with some orientations highlighted b.) Euler angles convention c.) Measured trajectories and errors.

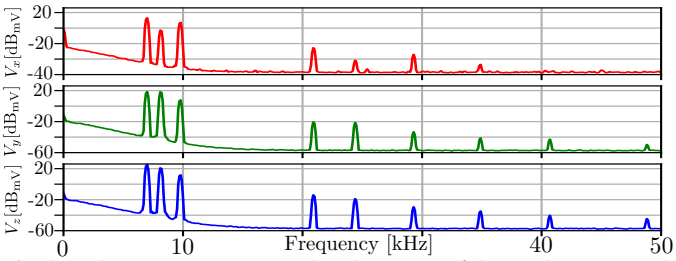

Fig. 8: Voltage spectra measured at the center of the workspace. RMS spectra for 2000-point DFTs sampled at 200 kHz.

the decrease in signal strength with the sensor area according to Eq. (5). In this case, the localization precision, defined as the standard deviation σ_p of the pose estimate, would change with the sensor size and the system parameters according to

$$\sigma_p \sim \frac{1}{\mathrm{SNR}} \sim \frac{\sqrt{R(N) f_{acq}}}{V_{DC} N A} \tag{15}$$

where A and N are the area and turns number of the coil and $f_{acq} = 1/T_{acq}$ is the frame acquisition rate. For sensors smaller than the ones used here, the loss in precision could be addressed by increasing the driving voltage from the 120 V used in this work.

IEEE Robotics and Automation Letters (RA-L) paper, presented at ICRA 2026, Vienna, Austria. Cite as RA-L paper.

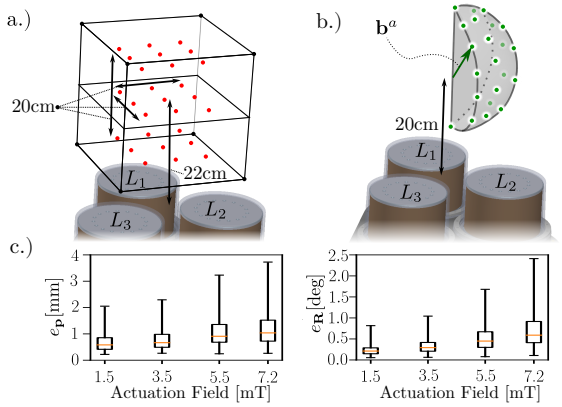

Fig. 9: Influence of actuation fields on the pose estimation accuracy. a.) Test location set b.) Applied actuation field directions c.) Measured position error distributions and orientation error distributions.

5) Influence of the Actuation Field: To measure the influence of an applied actuation field on the accuracy of the position estimate, the sensor was attached to the gantry stage used to acquire the calibration data, and the stage was driven to a test set of 27 different positions included in $\mathcal{V}$ (Fig. 9a). A set of actuation fields with different orientations and magnitudes was then applied at 20 cm from the coils (Fig. 9b). Fields of up to 7.2 mT in magnitude could be applied without running into limitations originating from the maximum available power or driver voltage. The position and orientation errors were measured for each applied field and at each grid position. The resulting error distributions are shown in Fig. 9c.

D. Actuation and Localization of a Magnetic Catheter

1) Navigation in Free Space: To evaluate the combined actuation and localization, the pickup coils and magnet depicted in Fig. 4d were embedded at the tip of a silicone tube with outer diameter 3.6 mm (Reichelt Chemietechnik No. 14242) to form a magnetic catheter, and the tip was covered with reflective tape for tracking with the OTS (see close-up in Fig. 10a). The catheter was placed in the workspace by fixing its base to the end-effector of the gantry stage (Fig. 10a). A rotating actuation field in the horizontal plane was then applied at a distance of 20 cm from the coils (see Fig. 10d) resulting in a motion of the catheter depicted in Fig. 10b. The height of the catheter was adjusted with the stage during the experiment. Figures 10c show the localized position coordinates for both the electromagnetic tracking and the ground truth obtained by the OTS. The mean position estimate accuracy was evaluated as 0.98 mm, where the position error was calculated using a Procrustes analysis without scaling. A correlation between catheter speed and localization error was observed with maximum positional errors occurring when the catheter was moving at the highest speed. A video of this experiment is available as a multimedia attachment to this article.

2) Navigation in an Anatomical Phantom: Combined actuation and localization of the magnetic catheter was finally demonstrated in a glass phantom of a human aortic arch and its supra-aortic vessels, a part of the anatomy that is typically navigated in interventional radiology. The magnetic

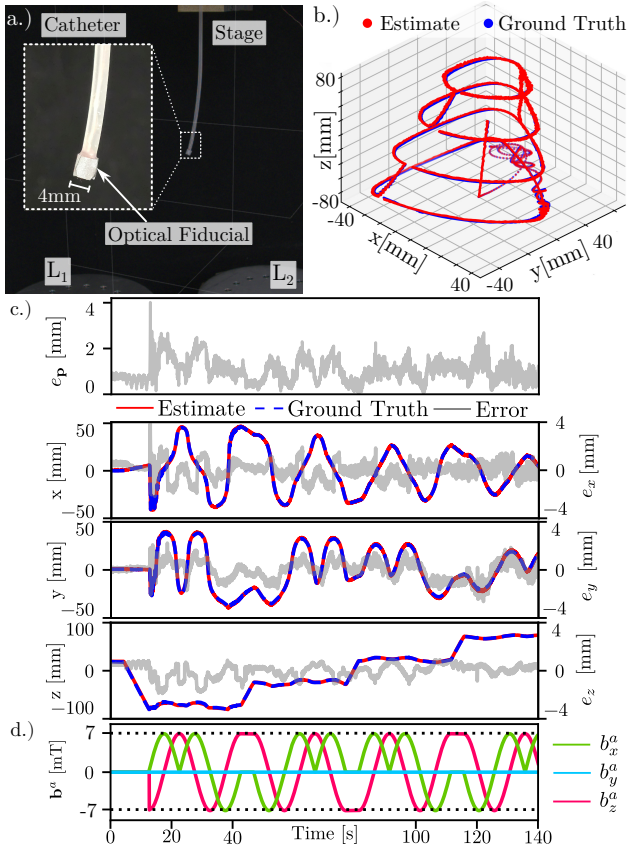

Fig. 10: Combined actuation and localization of a magnetic catheter in free space. a.) Experimental setup. b.) Estimated positions c.) Component-wise localization using optical tracking (ground truth) and electromagnetic tracking, with relative errors on each position coordinate d.) Applied actuation field components.

catheter was initially placed at the base of the aorta (Fig. 11a), and subsequently steered into two of the supra-aortic vessels (the left subclavian artery and the brachiocephalic trunk) by directing the catheter to a desired direction and advancing it using the gantry stage. Figures 11b-d illustrate the motion of the catheter through the model, and the localized trajectories during the experiment. A video of this experiment is available as a multimedia attachment to this article.

IV. Discussion and Conclusion

We introduced a method to estimate the pose of pickup coils embedded at the tip of a magnetic instrument that is actuated at the same time using an eMNS. The localization approach consists of measuring the ripple field of an eMNS created by orthogonal PWM signals driving the currents in its electromagnets. The field harmonics share a common oscillation period and uniquely identify the pose of the device to be localized. The pose was estimated at a rate of $1/3T = 77$ Hz in a volume of $(30\,\mathrm{cm})^3$ using a human-scale three-electromagnet eMNS. The method would allow for a maximum pose estimation rate of $1/T$, at the cost of a loss in precision according to Eq. (15). Typical mean estimation errors below 2 mm in position, and 2° in orientation were obtained with actuation fields of up to 7.2 mT. Compared to previous work using Hall effect sensors for combined actuation and localization with eMNS [11], the method presented in this work achieves better precision if the

IEEE Robotics and Automation Letters (RA-L) paper, presented at ICRA 2026, Vienna, Austria. Cite as RA-L paper.

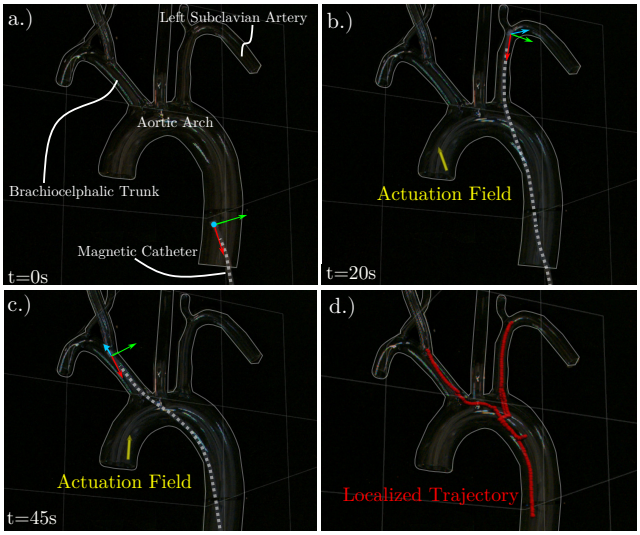

Fig. 11: Combined actuation and localization of a magnetic catheter in a vascular phantom. a.)-c.) Final poses of the catheter in two supra-aortic vessels d.) Estimated trajectory.

two methods are scaled to the same workspace and actuation magnet size and mitigates some challenges reported in [11] such as significant reactive power required to build up the localization fields and vibrations of the actuated magnet. The increase in the estimation error with actuation field magnitude observed in Section III-C5 was attributed to limitations of the LTI model assumed for the eMNS and the pickup coils (see Section II-D). More advanced eMNS modeling techniques were discussed in [18] for DC fields. Adaptation of such techniques for the AC ripple fields can be explored in the future to improve accuracy for higher actuation fields.

The proposed localization approach only relies on a single measurement from one sensor. To increase the robustness of the approach against external disturbances, the pose estimates of the method could be combined with advancer odometric data using a Kalman filter [19]. For the same reason, multiple pickup coil based sensors could be integrated into the device since the proposed method can localize an arbitrary number of sensors. The method was based on three pickups though six measurements from two pickups are theoretically sufficient to estimate the 6-DOF pose which will be investigated in future work. Like EMT methods, the approach is susceptible to errors due to metallic and ferromagnetic objects in the workspace as well as external magnetic fields that disturb the field harmonics [12]. This could be avoided by using non-metallic instruments in the workspace and changing PWM frequencies if necessary. The method proved robust against EMI emanating from the eMNS and laboratory environment.

We demonstrated navigation tasks both in free space and in a phantom of the aortic arch using a magnetic catheter with a diameter of $4\,\mathrm{mm}$. For a higher power eMNS such as [20] with a DC link voltage of $600\,\mathrm{V}$ and a sensor with a diameter of $2\,\mathrm{mm}$, the positional noise is expected to rise by 60% to $0.67\,\mathrm{mm}$. Such a system could also achieve higher bending radii of the catheter for applications such as PCI. Sensor miniaturization could be achieved by using a smaller actuation magnet and thinner wire for the pickup coils, similar to [21], which demonstrated usage of $12\,\mu\mathrm{m}$ wire for 3D pickup coils.

REFERENCES

[1] J. Hwang, J.-y. Kim, and H. Choi, "A review of magnetic actuation systems and magnetically actuated guidewire-and catheter-based microrobots for vascular interventions," *Intell. Serv. Robot.*, vol. 13, pp. 1–14, 2020.

[2] J. J. Abbott, E. Diller, and A. J. Petruska, "Magnetic methods in robotics," *Annu. Rev. Control Robot. Auton. Syst.*, vol. 3, pp. 57–90, 2020.

[3] K. M. Popek, T. Schmid, and J. J. Abbott, "Six-degree-of-freedom localization of an untethered magnetic capsule using a single rotating magnetic dipole," *IEEE Robot. Autom. Lett.*, vol. 2, no. 1, pp. 305–312, 2017.

[4] C. Di Natali, M. Beccani, and P. Valdastri, "Real-time pose detection for magnetic medical devices," *IEEE Trans. Magn.*, vol. 49, no. 7, pp. 3524–3527, 2013.

[5] C. Di Natali, M. Beccani, N. Simaan, and P. Valdastri, "Jacobian-based iterative method for magnetic localization in robotic capsule endoscopy," *IEEE Trans. Robot.*, vol. 32, no. 2, pp. 327–338, 2016.

[6] T. da Veiga, G. Pittiglio, M. Brockdorff, J. H. Chandler, and P. Valdastri, "Six-degree-of-freedom localization under multiple permanent magnets actuation," *IEEE Robot. Autom. Lett.*, vol. 8, no. 6, pp. 3422–3429, 2023.

[7] A. J. Sperry, J. J. Christensen, and J. J. Abbott, "Six-degree-of-freedom localization with a 3-axis accelerometer and a 2-axis magnetometer for magnetic capsule endoscopy," *IEEE Robot. Autom. Lett.*, vol. 7, no. 2, pp. 2110–2115, 2022.

[8] A. Z. Taddese, P. R. Slawinski, M. Pirotta, E. D. Momi, K. L. Obstein, and P. Valdastri, "Enhanced real-time pose estimation for closed-loop robotic manipulation of magnetically actuated capsule endoscopes," *Int. J. Robot. Res.*, vol. 37, no. 8, pp. 890–911, 2018.

[9] D. Son, S. Yim, and M. Sitti, "A 5-d localization method for a magnetically manipulated untethered robot using a 2-d array of hall-effect sensors," *IEEE/ASME transactions on mechatronics*, vol. 21, no. 2, pp. 708–716, 2015.

[10] C. Fischer, Q. Boehler, and B. J. Nelson, "Using magnetic fields to navigate and simultaneously localize catheters in endoluminal environments," *IEEE Robot. Autom. Lett.*, vol. 7, no. 3, pp. 7217–7223, 2022.

[11] D. von Arx, C. Fischer, H. Torlakcik, S. Pané, B. J. Nelson, and Q. Boehler, "Simultaneous localization and actuation using electromagnetic navigation systems," *IEEE Trans. Robot.*, vol. 40, pp. 1292–1308, 2024.

[12] A. M. Franz, T. Haidegger, W. Birkfellner, K. Cleary, T. M. Peters, and L. Maier-Hein, "Electromagnetic tracking in medicine—a review of technology, validation, and applications," *IEEE Trans. Med. Imaging*, vol. 33, no. 8, pp. 1702–1725, 2014.

[13] H. A. Jaeger, A. M. Franz, K. O'Donoghue, A. Seitel, F. Trauzettel, L. Maier-Hein, and P. Cantillon-Murphy, "Anser emt: the first open-source electromagnetic tracking platform for image-guided interventions," *Int. J. Comput. Assist. Radiol. Surg.*, vol. 12, pp. 1059–1067, 2017.

[14] M. Cavaliere, O. McVeigh, H. A. Jaeger, S. Hinds, K. O'Donoghue, and P. Cantillon-Murphy, "Inductive sensor design for electromagnetic tracking in image guided interventions," *IEEE Sens. J.*, vol. 20, no. 15, pp. 8623–8630, 2020.

[15] U. T. Koch, "Analysis of cricket stridulation using miniature angle detectors," *J. Comp. Physiol.*, vol. 136, no. 3, pp. 247–256, 1980.

[16] P. Merriaux, Y. Dupuis, R. Boutteau, P. Vasseur, and X. Savatier, "A study of vicon system positioning performance," *Sensors*, vol. 17, no. 7, p. 1591, 2017.

[17] F. C. Park, "Distance metrics on the rigid-body motions with applications to mechanism design," *J. Mech. Des.*, vol. 117, no. 1, pp. 48–54, 1995.

[18] S. L. Charreyron, Q. Boehler, B. Kim, C. Weibel, C. Chautems, and B. J. Nelson, "Modeling electromagnetic navigation systems," *IEEE Trans. Robot.*, vol. 37, no. 4, pp. 1009–1021, 2021.

[19] A. Dore, G. Smoljkic, E. V. Poorten, M. Sette, J. V. Sloten, and G.-Z. Yang, "Catheter navigation based on probabilistic fusion of electromagnetic tracking and physically-based simulation," in *2012 IEEE Int. Conf. Intell. Robots Syst.*, 2012, pp. 3806–3811.

[20] S. Gervasoni, N. Pedrini, T. Rifai, C. Fischer, F. C. Landers, M. Mattmann, R. Dreyfus, S. Viviani, A. Veciana, E. Masina *et al.*, "A human-scale clinically ready electromagnetic navigation system for magnetically responsive biomaterials and medical devices," *Adv. Mater.*, vol. 36, no. 31, p. 2310701, 2024.

[21] C. Schilstra and J. Van Hateren, "Using miniature sensor coils for simultaneous measurement of orientation and position of small, fast-moving animals," *J. Neurosci. Methods*, vol. 83, no. 2, pp. 125–131, 1998.